Intermittency measurement in two-dimensional bacterial turbulence

Xiang Qiu (邱翔),[1] Long Ding (丁龙),[1] Yongxiang Huang (黄永祥),[2,*] Ming Chen (陈铭),[2] Zhiming Lu (卢志明),[3]
Yulu Liu (刘宇陆),[3] and Quan Zhou (周全)[3]

[1]*School of Science, Shanghai Institute of Technology, Shanghai 200235, China*

[2]*State Key Laboratory of Marine Environmental Science, College of Ocean and Earth Sciences, Xiamen University,*
Xiamen 361102, People's Republic of China

[3]*Shanghai Institute of Applied Mathematics and Mechanics, Shanghai Key Laboratory of Mechanics in Energy Engineering,*
Shanghai University, Shanghai 200072, China

In this paper, an experimental velocity database of a bacterial collective motion, e.g., *Bacillus subtilis*, in turbulent phase with volume filling fraction 84% provided by Professor Goldstein at Cambridge University (UK), was analyzed to emphasize the scaling behavior of this active turbulence system. This was accomplished by performing a Hilbert-based methodology analysis to retrieve the scaling property without the β-limitation. A dual-power-law behavior separated by the viscosity scale ℓ_ν was observed for the qth-order Hilbert moment $\mathcal{L}_q(k)$. This dual-power-law belongs to an inverse-cascade since the scaling range is above the injection scale R, e.g., the bacterial body length. The measured scaling exponents $\zeta(q)$ of both the small-scale ($k > k_\nu$) and large-scale ($k < k_\nu$) motions are convex, showing the multifractality. A log-normal formula was put forward to characterize the multifractal intensity. The measured intermittency parameters are $\mu_S = 0.26$ and $\mu_L = 0.17$, respectively, for the small- and large-scale motions. It implies that the former cascade is more intermittent than the latter one, which is also confirmed by the corresponding singularity spectrum $f(\alpha)$ versus α. Comparison with the conventional two-dimensional Ekman-Navier-Stokes equation, a continuum model indicates that the origin of the multifractality could be a result of some additional nonlinear interaction terms, which deservers a more careful investigation.

I. INTRODUCTION

The most fascinating aspect of the hydrodynamic turbulence is its scale invariance, which is conventionally characterized by the qth-order structure functions,

$$S_q(\ell) = \langle |\Delta\mathbf{u}_\ell(\mathbf{x},t)|^q\rangle_{\mathbf{x},t} \sim \ell^{\zeta(q)}, \qquad (1)$$

where $\Delta\mathbf{u}_\ell(\mathbf{x},t) = \mathbf{u}(\mathbf{x}+\ell,t) - \mathbf{u}(\mathbf{x},t)$ is velocity increment of the Eulerian velocity field, ℓ is the separation scale, and $\langle\cdot\rangle_{\mathbf{x},t}$ means an ensemble average over $\mathbf{x}$ and t [1]. The separation scale ℓ should lie in the so-called inertial range $\ell_\nu \ll \ell \ll L$, where ℓ_ν is known as the Kolmogorov scale or viscosity scale, and L is the integral length scale. It was first introduced by Kolmogorov [2] in the year 1941 (K41 for short) with a nonintermittent scaling exponent $\zeta(q) = q/3$ [1]. The K41 theory is deeply related with an idea of energy cascade, which was first introduced phenomenologically by Richardson in the year 1922 [3]. The energy cascade has been interpreted as a main feature of the energy conservation law in the 3D turbulence, in which the energy is transferred from large-scale structures to small-scale ones, until the viscosity scale ℓ_ν, where the kinetic energy is converted into heat [1]. Generally, for a monofractal process, for instance fractional Brownian motion, a self-similarity process with stationary increments on different separation scales ℓ, the scaling $\zeta(q)$ is linear with q, e.g., $\zeta(q) = qH$, where H is the so-called Hurst number. However, for the high-Reynolds number turbulent flows, the experimental $\zeta(q)$ obtained from various experiments and numerics deviates from the K41

value $q/3$ [4–7]. A concept of multifractality and multiscaling is put forward to interpret this deviation [8,9]. It is further recognized as a main result of the energy dissipation field intermittency [1]. The "intermittent" or "intermittency" of the small-scale fluctuation was firstly noticed experimentally by Batchelor and Townsend [10]. It means a huge small-scale variation of the energy dissipation rate; see a nice example in Ref. [11, see Fig. 1] or in Ref. [12, see Figs. 2 and 3]. It is a result of strong nonlinear interactions in the Navier-Stokes equations. Several theoretical models have been put forward to describe the intermittent property of the energy dissipation field, for instance, the log-normal model [13], log-Poisson model [14,15], log-stable model [16,17], to list a few. Multifractality has also been recognized as a common feature of complex dynamic systems, such as financial activities [18–20], wind energy [21], geosciences [22,23], to name a few.

In the 2D turbulence, an additional enstrophy (i.e., the square of vorticity $\Omega = \frac{1}{2}\omega^2$) conservation is emerging below the forcing scale ℓ_F as a forward enstrophy cascade. On the other hand, above this forcing scale, the energy conservation leads to an inverse energy cascade, forming a remarkable large-scale motion, which could reach the system size [24]. Note that both the energy and enstrophy are injected into the system via the forcing scale ℓ_F. A 2D turbulence theory was put forward in 1967 by Kraichnan [25] to interpret this dual-cascade phenomenon. This 2D turbulence theory has been recognized as "one of the most important results in turbulence since Kolmogorov's 1941 work" [26]. More precisely, there is a forward enstrophy cascade with $E(k) \sim k^{-3}$ when $k_F \ll k \ll k_\nu$, in which k_F is the forcing wave number, and k_ν is the viscosity wave number where the enstrophy is

---

*yongxianghuang@gmail.com

dissipated; and there is an inverse cascade with $E(k) \sim k^{-5/3}$ when $k_\alpha \ll k \ll k_F$, in which k_α is the Ekman friction wave number [25,27]. This 2D turbulence theory has been partially confirmed by experiments and numerical simulations for the velocity field [27]. However, the statistics of the vorticity field shows inconsistence [28–30]. Concerning the multifractality, an extremely important feature of the turbulent systems, the inverse energy cascade is nonintermittent or anomaly free, which was confirmed by experiments not only using the velocity field [26,31] but also the vorticity field [30]. However, on the other hand, it has long been controversial whether or not the forward enstrophy cascade is intermittent since the classical structure function analysis fails to detect the scaling behavior when the slope of the Fourier power spectrum is $\beta \geqslant 3$ [1,32]. Nam *et al.* [33] theoretically showed that when the Ekman friction is present, the forward enstrophy cascade is then intermittent [34]. As already mentioned above this result is difficult to verify experimentally by using the conventional structure function analysis since the convergence condition requires the scaling exponent β of the Fourier spectrum, i.e., $E(k) \sim k^{-\beta}$, to be in the range (1,3) [1,12,32]; see also discussion in Sec. III. This is known as the β limitation. Recently, Tan, Huang, and Meng [30] applied the Hilbert-Huang transform, a method free with β limitation, to the vorticity field obtained from a high-resolution numerical simulation database with resolution 8192^2 grid points. They confirmed that the forward enstrophy cascade is intermittent, and the inverse cascade is nonintermittent. Wang and Huang [31] proposed a β-limitation free multilevel segment analysis and applied it to the 2D velocity field. They confirmed again that the forward enstrophy cascade is intermittent when considering the velocity statistics.

Specifically for a bacterial suspension in a thin fluid, if the considered spatial size is much larger than the thickness of the suspension, it could be approximated as a 2D fluid system. In such a system, the fluid is stirred by the bacterial activities at their body length R. Due to the hydrodynamic interaction or other mechanisms, the flow exhibits a turbulent-like movement, showing multiscale statistics [35–46]. Such flows are then called as bacterial turbulence or active turbulence. In this special flow system, the energy is injected into the system via the scale of the bacterial body length R typically around few μm [41]. The flow velocity is also of the order of a few μm per second. The corresponding Reynolds number is about Re $= O(10^{-3})$. In the traditional view of the classical hydrodynamic turbulence, the flow at such a low Reynolds number is laminar without turbulent-like statistics. It is surprising that the statistics of the active fluid exhibits a turbulent-like fluctuation, e.g., long-range correlation of velocity [37,39,40,42,45,47], power-law behavior [35,41,43,45,48], etc. For example, Wu and Libchaber reported that due to the collective dynamics of bacteria in a freely suspended soap film, the measured mean displacement function of beads demonstrates a superdiffusion in short times and normal diffusion in long times [35]. Wensink *et al.* [41] observed a dual-power-law (DPL) behavior in a quasi-2D active fluid. Due to the viscosity damping by the low-Re solvent, the experimental power-law behavior extends roughly up to $\ell_\nu \simeq 10R \simeq 50\,\mu$m, corresponding to a wave number $k_\nu/k_R \simeq 0.1$, where $k_R = 1/R$ is the wave number of

the bacterial body length, and ℓ_ν is the viscosity scale [49]. Above this wave number, e.g., $0.1 \leqslant k/k_R \leqslant 1$, one may has the energy-inertial regime of classical turbulence with a power-law roughly as $E(k) \sim k^{-8/3}$; and below it, e.g., $k/k_R \leqslant 0.1$, but not far from the viscosity scale k_ν, the viscous damping play an important role with a power-law that roughly can be fitted as $E(k) \sim k^{5/3}$ [41]. It is worth pointing out that these two power laws are on the same side of the injection scale R. Both of them belong to the inverse cascade. To the best of our knowledge, there are very few works related with the multifractality of the bacterial turbulence since the structure function analysis fails to capture the scaling behavior. Liu and I [48] experimentally found that the multifractality revealed by the extended self-similarity (ESS) technique is increasing with the cell concentration. Note that in the ESS approach, instead of plotting the qth-order structure function $S_q(\ell)$ versus the separation scale ℓ, the experimental $S_q(\ell)$ is often plotted against with $S_2(\ell)$ or $S_3(\ell)$ [50]. It provides a more robust way to extract the scaling exponent $\zeta(q)$ [51–53]. With the help of ESS, the relative scaling exponent is found to be universal for a large range of Reynolds number and the statistics order q up to 10 [51].

In this paper, we investigated the multifractality of the bacterial turbulence experimentally using the Hilbert-Huang transform to identify the power-law behavior and extract scaling exponent $\zeta(q)$ directly without resorting to the ESS technique. It is found that the intermittent correction is relevant in the observed DPL. The corresponding intermittency parameter provided by a log-normal formula is $\mu_S = 0.26$ and $\mu_L = 0.17$, respectively, for the small-scale fluctuations above the viscosity scale and the large-scale fluctuations below the viscosity scale. The observed multifractality could be a result of the several additional nonlinear terms appearing in an Ekman-Navier-Stokes-like model equation [41].

II. EXPERIMENTAL DATA

The experiment data analyzed here is provided by Professor R. E. Goldstein at Cambridge University (UK). We recall briefly the main parameters of this quasi-2D experiment in a microfluidic chamber. The bacteria used in this experiment is *Bacillus subtilis* with an individual body length approximately $5\,\mu$m, in which the energy is injected into the system. The volume-filling fraction is $\phi = 84\%$ with bacterial number $N \simeq 9968$ and aspect ratio $a = 5$, i.e., the ratio between the bacterial body length R and the body diameter. The quasi-2D microfluidic chamber is with a vertical height H_c less or equal to the individual body length of *B. subtilis* (approximately $5\,\mu$m). With these parameters, the flow is then in a turbulent phase [41]. The PIV (particle image velocimetry) measurement area is $217\,\mu$m $\times$ $217\,\mu$m. The image resolution is of 700 pix $\times$ 700 pix with conversion rate $0.31\,\mu$m/pix and frame rate 40Hz. The commercial PIV software Dantec Flow Manager is used to extract the flow-field component with a moving window size 32 pix $\times$ 32 pix and 75% overlap. This results a 84×84 velocity vector and a total 1015 snapshots, corresponding to a time period ~ 25 s. Therefore, totally we
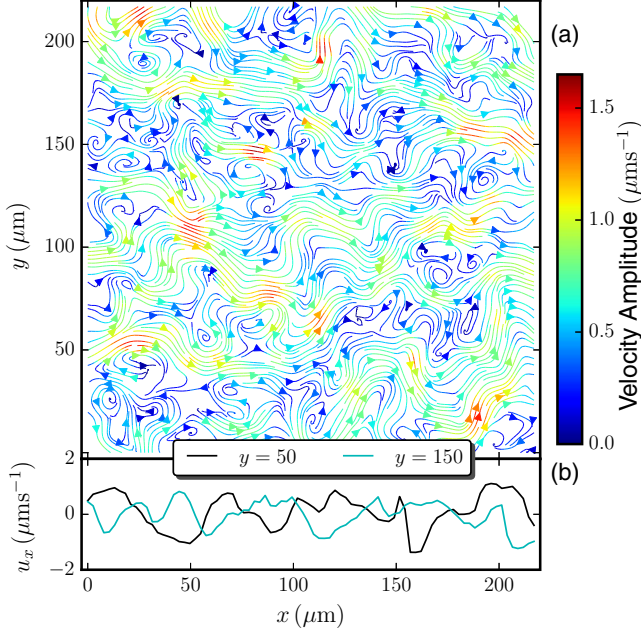
FIG. 1. (a) A snapshot of the velocity streamline, which is color encoded by the velocity amplitude. (b) The velocity $u_x(x)$ at $y = 50\,\mu$m and $y = 150\,\mu$m. Energetic structures are observed roughly with a spatial scale $\sim 50\,\mu$m, corresponding to 10 times of the bacterial body size R.

have 7 161 840 data points, which ensures a good statistics at least up to the statistical order $q = 4$.

Figure 1(a) shows a snapshot of the streamline, where the velocity amplitude is encoded in color. Figure 1(b) shows the velocity $u_x(x|y)$ slice at $y = 50$ and $150\,\mu$m. Visually, we observe energetic structures roughly with a spatial scale $\sim 50\,\mu$m, corresponding to ten times of the bacterial body size, i.e., $10R$. The origin of this structure is unclear. We will turn back to this point in Sec. VI. The flow field is homogeneous and isotropic. In the following analysis, only the

velocity component $u_x(x,y,t)$ is considered. It is first divided into 84 lines along the direction x. Statistical quantities are then estimated for all snapshots.

III. SCALE MIXTURE PROBLEM OF STRUCTURE FUNCTION ANALYSIS

We show here the scale mixture problem of the conventional structure function analysis. The second-order structure function $S_2(\ell)$ can be associated with the Fourier power spectrum $E(k)$ via the Wiener-Khinchin theorem [1,12],

$$S_2(\ell) = \int_0^{+\infty} E(k)[1 - \cos(2\pi k\ell)]dk, \qquad (2)$$

where ℓ is the separation scale, and k is the wave number. A prefactor is ignored. It implies that except for the case $k = n/\ell, n = 0,1,2,\ldots$, all Fourier components have contribution to $S_2(\ell)$. Or in other words, it contains information from different Fourier components [32]. Taking a pure power-law form $E(k) \sim k^{-\beta}$, the convergence conditions at $k \to 0$ and $k \to +\infty$ require $\beta \in (1,3)$ [1,12,32]. Unfortunately, if the data set has energetic structures, the structure function analysis will be strongly biased. For instance, the ramp-cliff structure in the passive scalar turbulence [32,54], vortex trapping event in the Lagrangian velocity [55], high-intensity vortex in 2D turbulence [30,31], daily cycle or annual cycle in the collected geosciences data [22], to list a few. Therefore, before applying the structure function analysis, as we will show below, it is better to perform a scale-by-scale analysis to see whether such influence exists or not. To characterize quantitatively the relative contribution of different Fourier components, we introduced here a contribution kernel function $\mathcal{I}(k,\ell)$,

$$\mathcal{I}(k,\ell) = \frac{E(k)[1 - \cos(2\pi k\ell)]}{S_2(\ell)}, \qquad (3)$$

where $E(k)$ is the Fourier power spectrum provided by the experimental velocity field. Figure 2(a) shows the experimental $\mathcal{I}(k,\ell)$, in which the power-law range $0.03 < k/k_R < 0.075$ and $0.15 < k/k_R < 0.5$ (see analysis result in Sec. V) are
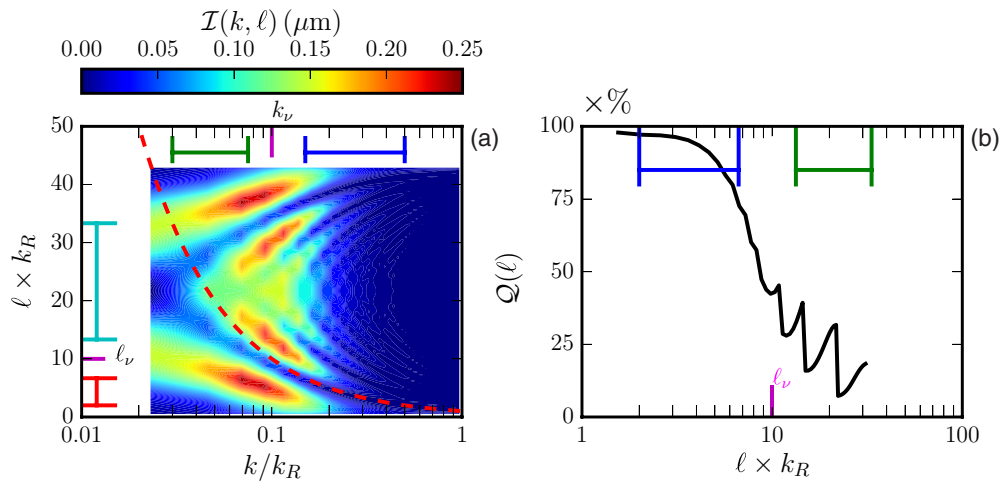

FIG. 2. (a) The experimental contribution kernel $\mathcal{I}(k,\ell)$, in which the range of the dual-power-law is indicated by horizontal lines. The peak location (the viscosity scale) of the Fourier power spectrum $E(k)$ is indicated by k_ν, corresponding to a spatial scale $\ell_\nu = 1/k_\nu$. The dashed line illustrates $\ell = 1/k$. (b) The measured large-scale contribution $\mathcal{Q}(\ell) = \int_0^{1/\ell} \mathcal{I}(k,\ell)dk$.

illustrated by solid lines. The dashed line indicates $\ell = 1/k$. Visually, most of the contribution is coming from the large-scale part, i.e., $k/k_R \leqslant 0.2$. It also displays an up-down symmetry. This is because the Fourier power spectrum $E(k)$ increasing with k when $k/k_R \leqslant 0.1$ and taking its peak at $k/k_R \simeq 0.1$; see Fig. 5(a). A relative cumulative function is introduced to characterize the relative contribution from the large-scale part,

$$\mathcal{Q}(\ell) = \int_0^{1/\ell} \mathcal{I}(k,\ell) dk \times 100\%. \tag{4}$$

Figure 2(b) shows the measured $\mathcal{Q}(\ell)$, in which the expected power-law range is indicated by solid line. Experimentally, $S_2(\ell)$ in the first power-law range, i.e., $0.15 < k/k_R < 0.5$, is strongly influenced by the large-scale motions; in the second power-law range, i.e., $0.03 < k/k_R < 0.075$, it is strongly influenced by the energetic structures around $k/k_R \simeq 0.1$. Due to the presence of energetic structures, the expected power-law behavior is then destroyed or biased in the physical domain [41]. A similar phenomenon has been observed for the vorticity field of the traditional 2D turbulence with high-intensity vortex structures [30], and for passive scalar turbulence with ramp-cliff structures [32], etc. For more details about this topic, we refer the readers to Ref. [12].

IV. HILBERT-HUANG TRANSFORM

In this work, we will employ a β-limitation free approach, namely Hilbert-Huang transform [56,57]. It has the capability to isolate different events not only in the physical domain but also in spectral space [12,30,54,55]. This method consists two steps: (i) empirical mode decomposition (EMD), and (ii) Hilbert spectral analysis. In the following, we present more details of this Hilbert-based approach.

A. Empirical mode decomposition

In reality, most of the collected signals are multicomponent, which means that different time or space scales are coexistent [56,58]. It is thus necessary to apply a proper method to separate a given signal into a sum of monocomponents to have a better view of them. For example, in the classical Fourier analysis, a trigonometric function sine or cosine is chosen as the monocomponent [59]. The given data set is then associated with the energy (the square of the amplitude) and the wave number (the inverse of the period of the given sine or cosine wave), known as the Fourier power spectrum.

In this Hilbert-based approach, the so-called intrinsic mode function (IMF) has been put forward to represent the monocomponent, which satisfies the following two conditions: (i) the difference between the number of local extrema and the number of zero-crossings must be zero or one; (ii) the running mean value of the envelope defined by the local maxima and the envelope defined by the local minima is zero [56,60]. Each IMF then has a well-defined Hilbert spectrum [56]. It allows both the amplitude- and frequency or wave-number-modulation simultaneously since its characteristic scale is defined as the distance between two successive extreme points [61].

The empirical mode decomposition algorithm is put forward to extract the IMF modes from a given data set, e.g.,

velocity $u(x)$. The first step of the EMD algorithm is to identify all the local maxima (minima) points. Once all the local maxima points are identified, the upper envelope $e_{\max}(x)$ (lower envelope $e_{\min}(x)$) is constructed by a cubic spline interpolation [56,58,62]. Note that other approaches are also possible to construct the envelope [63]. The running mean between these two envelopes is defined as

$$m_1(x) = \frac{[e_{\max}(x) + e_{\min}(x)]}{2}. \tag{5}$$

The first component is estimated as

$$h_1(x) = u(x) - m_1(x). \tag{6}$$

Ideally, $h_1(x)$ should be an IMF as expected. In reality, however, $h_1(x)$ may not satisfy the condition to be an IMF. We take $h_1(x)$ as a new data series and repeat the sifting process j times, until $h_{1j}(x)$ is an IMF. We thus have the first IMF component,

$$C_1(x) = h_{1j}(x), \tag{7}$$

and the residual,

$$r_1(x) = u(x) - C_1(x). \tag{8}$$

The sifting procedure is then repeated on residuals until $r_n(x)$ becomes a monotonic function or at most has one local extreme point. This means that no more IMF can be extracted from $r_n(x)$. Thus, with this algorithm we finally have n IMF modes with one residual $r_n(x)$. The original data $u(x)$ is then rewritten as

$$u(x) = \sum_{i=1}^{n} C_i(x) + r_n(x). \tag{9}$$

A stopping criterion has to be introduced in the EMD algorithm to stop the sifting process [56,58,60,64]. The first stopping criterion is a Cauchy-type convergence criterion proposed by Huang *et al.* [56]. A standard deviation defined for two successive sifting processes is written as

$$\mathrm{SD} = \frac{\sum_{x=0}^{L} |h_{i(j-1)}(x) - h_j(x)|^2}{\sum_{x=0}^{L} h_{i(j-1)}^2(x)}, \tag{10}$$

in which L is the total length of the data. If a calculated SD is smaller than a given value, then the sifting stops and gives an IMF. A typical value $\mathrm{SD} \in [0.2, 0.3]$ has been proposed based on Huang *et al.*'s experiences [56,58]. Another widely used criterion is based on three thresholds, α, θ_1, and θ_2, which are designed to guarantee globally small fluctuations, meanwhile taking into account locally large excursions [60]. The mode amplitude and evaluation function are given as

$$a(x) = \frac{e_{\max}(x) - e_{\min}(x)}{2}, \quad \sigma(x) = |m(x)/a(x)| \tag{11}$$

so that the sifting is iterated until $\sigma(x) < \theta_1$ for some prescribed fraction $1 - \alpha$ of the total duration, while $\sigma(x) < \theta_2$ for the remaining fraction. Typical values proposed in Ref. [60] are $\alpha \approx 0.05$, $\theta_1 \approx 0.05$, and $\theta_2 \approx 10\theta_1$, respectively, based on their experience. In practice, a maximal iteration number (e.g., 300) is also chosen to avoid over-decomposing the data set.

A main drawback of this method is that EMD is an algorithm in practice without rigorous mathematical foundation [56]. Several works attempt to understand better the mathematical aspect of EMD algorithm [60,62,65–68]. For instance, Flandrin and Gonçalvès [62] found that the EMD algorithm acts as a data-driven wavelet-like expansion. Wang *et al.* [67] reported that both the time and space complexity of the EMD algorithm are $O(n \cdot \log n)$, in which n is the data size, but with a larger factor than the traditional Fourier transform.

B. Hilbert spectral analysis

With the achieved IMF modes, the Hilbert spectral analysis is then applied to each $C_i(x)$ to retrieve the spectral information via the classical Hilbert transform,

$$\overline{C}_i(x) = \frac{1}{\pi} P \int \frac{C_i(x')}{x - x'} dx', \qquad (12)$$

in which P means the Cauchy principal value. An analytical signal is then reconstructed as

$$C_i^A(x) = C_i(x) + j\overline{C}_i(x) = \mathcal{A}_i(x) \exp[j\phi_i(x)], \qquad (13)$$

in which $j = \sqrt{-1}$, $\mathcal{A}_i(x)$ is the amplitude, and $\phi_i(x)$ is the phase function, which are, respectively, defined as

$$\mathcal{A}_i(x) = |C_i^A(x)| = \sqrt{C_i(x)^2 + \overline{C}_i(x)^2}, \qquad (14)$$

for the amplitude, and

$$\phi_i(x) = \arctan\left[\frac{\overline{C}_i(x)}{C_i(x)}\right], \qquad (15)$$

for the phase function. An instantaneous wave number is then defined as

$$k_i(x) = \frac{1}{2\pi} \frac{d\phi_i(x)}{dx}. \qquad (16)$$

Note that the EMD decomposes the given signal very locally into several IMF modes, and the above-described HSA approach extracts the instantaneous amplitude $\mathcal{A}_i(x)$ and wave number $k_i(x)$ also at a very local level. The EMD-HSA approach thus inherits a very local ability, namely the amplitude- and frequency or wave-number modulation to characterize the nonlinear and nonstationary properties of the data collected from the real world [12,56,58].

To show the capability of the EMD-HSA approach, we consider here a toy model with two components on the range $-10 \leqslant x \leqslant 10$,

$$z(x) = z_1(x) + z_2(x), \quad z_1(x) = \sin(x^2), \quad z_2(x) = x^2/20. \qquad (17)$$

The first component $z_1(x)$ has an instantaneous wave number $k(x) = |(x)|/2\pi$. After the EMD, one IMF mode $C_1(x)$ with one residual $r_1(x)$ are obtained. Figure 3(a) shows the toy model $z(x)$, and Fig. 3(b) shows $C_1(x)$, $r_1(x)$ (thin lines), $z_1(x)$, and $z_2(x)$, respectively. Visually, except for the range $-2 < x < 2$, two components are well separated by the EMD algorithm. The instantaneous wave number $k(x)$ is retrieved by applying Eqs. (12)~(16). Note that the estimated $k(x)$ agrees with the theoretical one very well, showing the very local capability of the EMD-HSA approach.
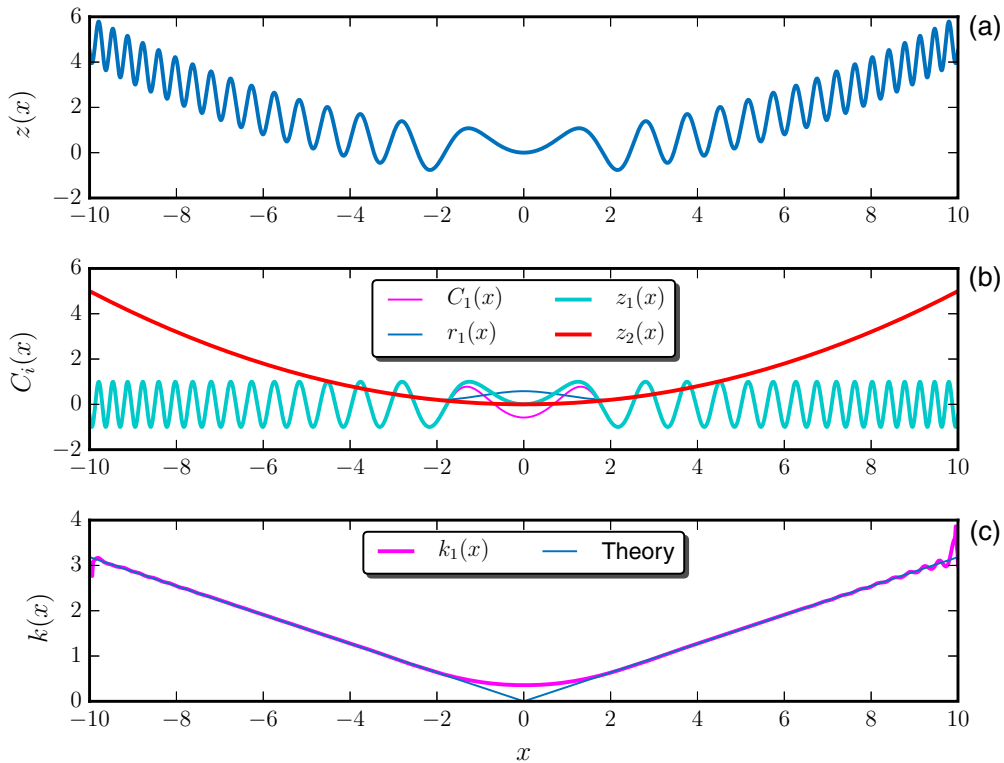

FIG. 3. (a) Illustration of a toy model $z(x) = z_1(x) + z_2(x)$, where $z_1(x) = \sin(x^2)$ and $z_2(x) = x^2/20$. (b) IMF mode $C_1(x)$ and residual $r_1(x)$ obtained from EMD algorithm (thin lines). For comparison, the $z_1(x)$ and $z_2(x)$ are also shown (thick lines). (c) The measured instantaneous wave number $k(x)$ for $C_1(x)$ (thick line), where the theoretical value is shown as a thin line.

C. Hilbert-based high-order statistics

One can construct pairs of the instantaneous wave number and amplitude, i.e., $[k_i(x), \mathcal{A}_i(x)]$ for all IMF modes. A joint probability density function (pdf) $p(k, \mathcal{A})$ is then extracted from all IMF modes [12,57]. A k-condition qth-order statistics is defined as

$$\mathcal{L}_q(k) = \left\langle \sum_i \mathcal{A}_i^q(x) | k_i(x) = k \right\rangle_{x,t}, \qquad (18)$$

where $\langle \cdot \rangle_{x,t}$ means an ensemble average over space and time. In case of scale invariance, one has power-law behavior,

$$\mathcal{L}_q(k) \sim k^{-\zeta(q)}, \qquad (19)$$

in which $\zeta(q)$ is the Hilbert-based scaling exponent. For a simple scaling process, such as fractional Brownian motion, the measured $\zeta(q)$ is equivalent to the one provided by the structure function analysis [12,55,57]. For a real data with energetic structures, this approach has a capability to isolate those structures to reveal more accurate scaling behavior [12,30,32,55]. For more details about the EMD-HSA method, we refer to Refs. [12,56,58].

V. RESULTS

In the following the analysis is done along x direction by dividing the Eulerian velocity $\mathbf{u}(x, y)$ into 84 lines. The EMD-HSA approach is then performed to each slice and the statistics are then averaged over these 84 lines and all snapshots.

Figure 4(a) shows the measured joint-pdf $p(k, \mathcal{A})$, in which the horizontal axis is normalized by the wave number k_R of the bacterial body length. For display convenience, the measured $p(k, \mathcal{A})$ has been represented in log scale. A DPL trend is visible, respectively, on the range $0.15 < k/k_R < 0.5$ for the small-scale structures, and $0.03 < k/k_R < 0.075$ for the large-scale structures. The scaling trend is characterized

by a skeleton, which is defined as

$$p_{\max}(k) = p(k, \mathcal{A}_S(k)) = \max_{\mathcal{A}} \{p(k, \mathcal{A})|_k\}, \qquad (20)$$

The measured $\mathcal{A}_S(k)$ is reproduced in Fig. 4(b). The DPL behavior is identified,

$$\mathcal{A}_S(k) \sim k^{-\gamma}, \qquad (21)$$

in which γ is the scaling exponent. Figure 4(b) reproduces the measured $\mathcal{A}_S(k)$, showing the DPL behavior. The experimental scaling exponents are respectively $\gamma_S = 0.95 \pm 0.02$ for the small-scale structures, and $\gamma_L = -0.95 \pm 0.02$ for the large-scale structures. To emphasize the observed power-law behavior, the compensated curve is shown as the inset in Fig. 4(b). A clear plateau confirms the existence of the power-law behavior. The peak location (the viscosity wave number k_ν) in Fig. 4(b) is to be around $k_\nu/k_R \simeq 0.1$, which agrees very well with the observation of the Fourier power spectrum [41]; see also Fig. 5(a).

Figure 5(a) shows the measured energy spectrum provided by the Fourier analysis (○) and the Hilbert spectral analysis (□). The DPL predicted by the Hilbert spectrum is indicated by the horizontal dashed line, respectively, on the range $0.03 < k/k_R < 0.075$ and $0.15 < k/k_R < 0.5$. To emphasize the observed DPL, the compensated curve, e.g., $E(k)k^\beta C^{-1}$, using the fitted scaling exponent β and the prefactor C is shown in Fig. 5(b). The fitted scaling exponents are $\beta_S^F = 2.68 \pm 0.06$, $\beta_L^F = -1.33 \pm 0.20$ provided by the Fourier spectrum, and $\beta_S^H = 2.64 \pm 0.05$, $\beta_L^H = -0.41 \pm 0.05$ provided by the Hilbert spectrum, respectively. The observed plateau in Fig. 5(b) confirms again the existence of the DPL behavior at least for the second-order statistics. The statistics of the small-scale fluctuations (the high wave-number part) by the Fourier and Hilbert agree well with each other. However, the ones of the large-scale fluctuations (low wave-number part) do not agree. One possible reason might be the nonlinear distortion embedded in the data [56]. Moreover, the DPL is separated by a peak around $k_\nu/k_R \simeq 0.1$, which corresponds to
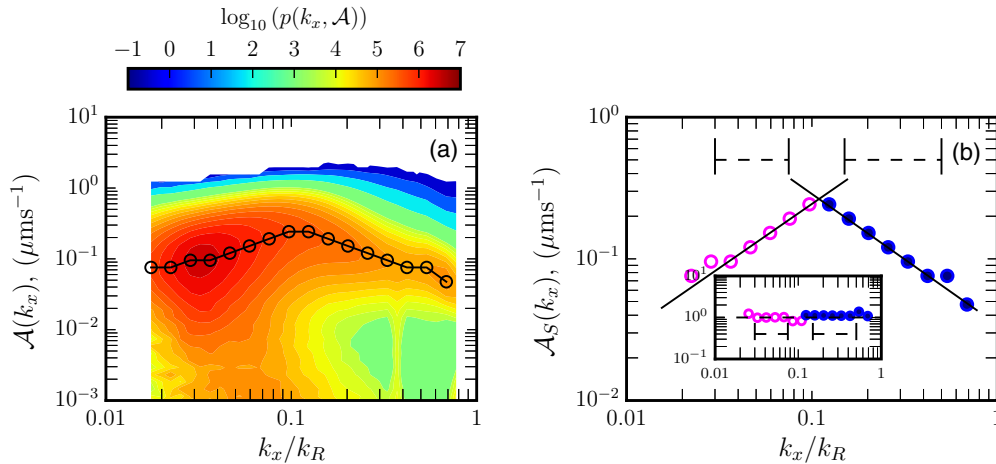

FIG. 4. (a) Measured joint-pdf $p(k, \mathcal{A})$ of the wave number k and amplitude $\mathcal{A}$. A skeleton defined by Eq. (20) is illustrated by ○, showing a scaling trend. The horizontal axis is normalized by the wave number of the bacterial length, i.e., k_R. (b) Reproduce the measured skeleton $\mathcal{A}_S(k)$ of the joint-pdf $p(k, \mathcal{A})$. A dual-power-law behavior $\mathcal{A}_S(k) \sim k^{-\gamma}$ is visible with scaling exponents -0.95 ± 0.02 and 0.95 ± 0.02 on the range $0.15 < k/k_R < 0.5$ for the small-scale structures and $0.03 < k/k_R < 0.075$ for the large-scale structures. The inset shows the compensated curve to emphasize the observed power-law behavior.
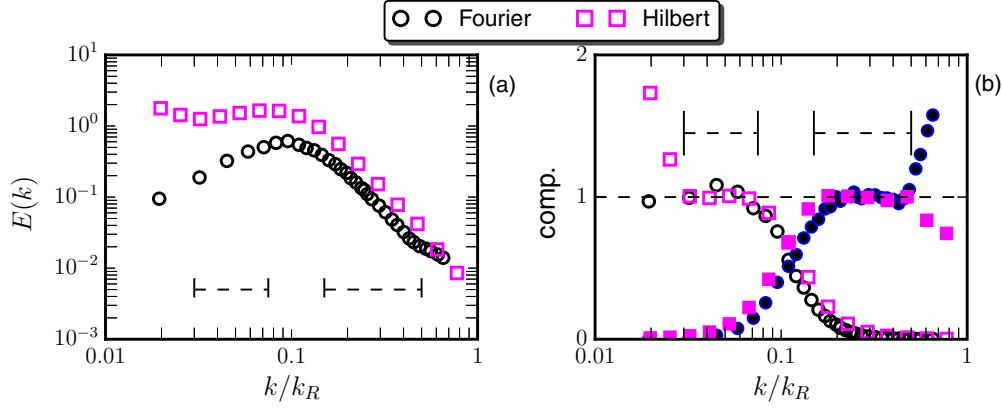
FIG. 5. (a) Comparison of the experimental energy spectra $E(k)$ provided by the Fourier analysis ($\circ$) and Hilbert spectral analysis ($\square$). For display convenience, the curve has been vertically shifted. (b) The compensated curves using the fitted scaling exponents, respectively, $\beta_S^F = 2.68 \pm 0.06, \beta_L^F = -1.33 \pm 0.20$, provided by the Fourier spectrum, and $\beta_S^H = 2.64 \pm 0.04, \beta_L^H = -0.41 \pm 0.05$, provided by the Hilbert spectrum. The power-law range predicted by the Hilbert approach is indicated by the horizontal dashed line for the range $0.15 < k/k_R < 0.5$ of the small-scale structures and $0.03 < k/k_R < 0.075$ of the large-scale structures.

the scale of the fluid viscosity. The observed power-law range is limited due to the constrain of this system, e.g., injection scale R, the fluid viscosity k_v, the measurement area L, etc.

Note that the power-law behavior of the measured spectrum often indicates a cascade process. As an analogy to the 2D turbulence theory, we speculate that at least the energy transfers from the injected scale R to larger-scale structures via an inverse cascade. As mentioned above, due to the fluid viscosity, the energy is then accumulated around $k/k_R \simeq 0.1$. This postulation should be verified carefully via a scale-to-scale energy or enstrophy flux [69]. Below we check the high-order statistics to see potential intermittent correction.

Figure 6 shows the measured high-order Hilbert moments $\mathcal{L}_q(k)$ for $0 \leqslant q \leqslant 4$. The DPL behavior is observed for all q considered here. The power-law ranges are the same as the ones observed in Fig. 5. The corresponding scaling exponents are then estimated using a least-square fitting algorithm. The measured $\zeta(q)$ are shown in Fig. 7(a). The error bar indicates the 95% confidence interval provided by the fitting algorithm. Visually, the experimental scaling exponent curves

are convex, implying multifractal nature of this active system. To characterize the intensity of multifractality quantitatively, we introduce here a log-normal formula to fit the observed scaling exponent,

$$\zeta(q) = qH - \frac{\mu}{2}(q^2H^2 - qH), \tag{22}$$

where H is the Hurst number, and μ is the intermittency parameter [20]. Note that the log-normal model was first introduced by Kolmogorov [13] in 1962 for the Eulerian velocity by assuming a log-normal distribution of the energy dissipation field. It yields for the turbulent velocity $\zeta(q) = q/3 - \mu/2(q^2/9 - q/3)$ [1,12]. For a given H, the intermittency parameter μ characterizes the deviation from the linear relation qH. Or in other words, a larger value of μ has, the more intermittent the field is. The measured Hurst number and intermittency parameter are $H_S = 0.91 \pm 0.02$ and $\mu_S = 0.26 \pm 0.01$ for $\zeta_S(q)$, and $H_L = 0.73 \pm 0.01$ and $\mu_L = 0.17 \pm 0.01$ for $-\zeta_L(q)$, respectively. It shows a more intermittent small-scale fluctuations.
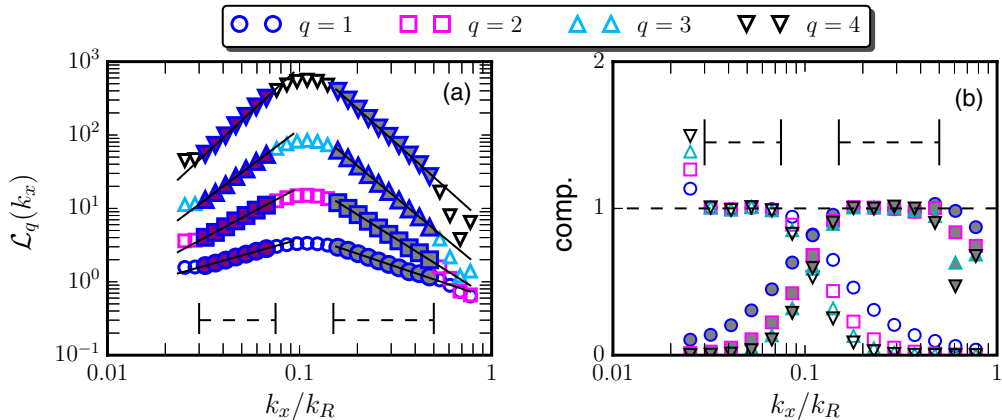

FIG. 6. (a) Measured qth-order Hilbert moment $\mathcal{L}_q(k)$. (b) The corresponding compensated curve using the fitted scaling exponent and prefactor. A double power-law behavior is observed on the range $0.03 < k/k_R < 0.075$ and $0.15 < k/k_R < 0.5$. The existence of the plateau confirms the observed power-law behavior. The scaling exponent is then estimated on these ranges using a least-square fitting algorithm.
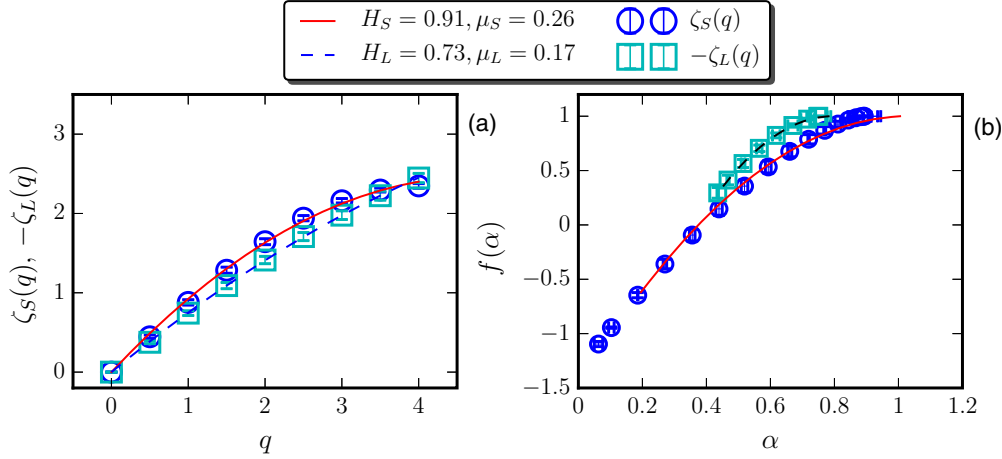
FIG. 7. (a) Experimental scaling exponent $\zeta(q)$ for the small-scale scaling ($\circ$) and large-scale scaling ($\square$). A log-normal formula fitting is also shown as solid and dashed lines, respectively, for the small and large scales. (b) The corresponding singularity spectrum $f(\alpha)$ versus α. The error bar indicates the 95% confidence interval provided by the least-square fitting algorithm.

VI. DISCUSSIONS

There are two free parameters in Eq. (22). Therefore, a different choice of H could lead to a different estimated intermittent parameter μ. To avoid this difficulty, we consider below the singularity spectrum $f(\alpha)$ via the Legendre transform,

$$\alpha = \frac{d\zeta(q)}{dq}, \quad f(\alpha) = \min_q\{\alpha q - \zeta(q) + 1\}, \quad (23)$$

in which α is known as the generalized Hurst number or intensity of multifractality [1]. Generally, the broader measured α and $f(\alpha)$ are the more the experiment $\zeta(q)$ deviates from a linear relation qH even the Hurst number H cannot be accessed precisely. Thus, the analyzed field is more intermittent [1]. Figure 7(b) shows the measured $f(\alpha)$ versus α. A broad range of α and $f(\alpha)$ is observed, suggesting that both small-scale and large-scale fluctuations possessing intermittent correction, while the former one is more intermittent than the latter one, which confirms the result of the log-normal formula fitting.

We would like to provide some comments on the finite scaling range detected by the Hilbert method. In this special dynamic system, the scaling range is determined by several parameters. They are, at least, the bacterial body length $R \simeq 5\,\mu$m, where the energy is injected into the system; the size of the microfluidic device or the measurement area $L \times L$ with $L \simeq 217\,\mu$m for the current data set; the fluid viscosity scale $\ell_\nu \simeq 50\,\mu$m, below which a part of the kinetic energy might be dissipated into heat; the Ekman-like friction provided by interface between the fluid and the bottom of the microfluidic device and other unknown mechanisms, in which the energy is damped, etc. Note that the fluid viscosity could be also a function of species and concentrations of bacteria [70–72]. The scaling range of such bacterial turbulence is thus limited due to these length scales. For instance, the scaling ranges identified in this work are, respectively, $0.03 < k/k_R < 0.075$ and $0.15 < k/k_R < 0.5$, corresponding to roughly $\simeq 0.4$ and $\simeq 0.5$ decades. For the former scaling range, it could be limited by the size of the microfluidic device and the fluid viscosity, i.e., $\ell_\nu \simeq 10R$ or $k_\nu \simeq 0.1k_R$. It thus could be extended by

increasing the measurement area. The latter one is constrained not only by the fluid viscosity, but also by the bacterial body length R and the depth of the fluid H_c. For the spatial scale comparable with the fluid depth H_c, the motion could exhibit 3D statistics. It seems that it is difficult to extend this scaling range by simply increasing the measurement resolution or reducing the bacterial body length R since the fluid viscosity is a function of bacterial concentrations and other conditions [70–72].

Moreover, the observed DPL is on the left side of the injection scale. It is therefore then inverse cascade, at least in the sense of the kinetic energy. In the view of the traditional 2D turbulence, the inverse energy cascade is found to be nonintermittent [27]. The corresponding forward enstrophy cascade is intermittent if the Ekman friction is present [33], which has been confirmed for both the vorticity field [30] and the velocity field [31]. The Ekman-Navier-Stokes equation for the classical 2D turbulence is written as

$$\partial_t \mathbf{u} + \mathbf{u} \cdot \nabla\mathbf{u} = -\nabla p + \nu\nabla^2\mathbf{u} - \xi\mathbf{u} + \mathbf{f}_u, \quad (24)$$

in which ξ stands for the Enkman friction coefficient, and $\mathbf{f}_u$ is the external forcing, where the energy and enstrophy are injected into the system. Note that the Ekman friction is a linear drag to model the three-dimension of no-slip boundary condition or the effect of the boundary layer itself in the two-dimensional description. The dual-cascade theory proposed by Kraichnan has been proved partially by the experiments and numerical simulations [27]. A continuum model has been put forward to model the bacterial turbulence, which is written as

$$\partial_t \mathbf{u} + \lambda_0\mathbf{u} \cdot \nabla\mathbf{u} = -\nabla p + \Gamma_0\nabla^2\mathbf{u} + \lambda_1\nabla\mathbf{u}^2$$
$$- (\varpi + \chi|\mathbf{u}|^2)\mathbf{u} - \Gamma_2(\nabla^2)^2\mathbf{u}, \quad (25)$$

where p denotes pressure, and $\lambda_0 > 1$; $\lambda_1 > 0$ for the pusher-swimmers as used in this study; (ϖ, χ) corresponds to a quartic Landau-type velocity potential; (Γ_0, Γ_2) provides the description of the self-sustained mesoscale turbulence in incompressible active flow, e.g., $\Gamma_0 < 0$ and $\Gamma_2 > 0$, the model results in a turbulent state [41]. Comparing the righthand side of Eqs. (25) and (24), one can find that in the continuum

theory several additional nonlinear interaction terms are introduced. We speculate here that these additional nonlinear interactions trigger the intermittency effect into the inverse cascade of the bacterial turbulence, which is different with the traditional two-dimensional turbulence and deserves a further careful investigation by checking the scale-to-scale energy and enstrophy flux of this active system.

VII. CONCLUSION

In summary, in this paper the experimental Eulerian velocity of the bacterial turbulence provided by Professor Goldstein at Cambridge University (UK) was analyzed to emphasize on the multiscaling property. A kind of bacteria *B. subtilis* with a body size of 5 μm is used in this experiment with a volume filling fraction 84% and a finite depth of $\simeq 5$ μm. With these parameters, the active flow is in the turbulent phase. Due to the scale mixture problem, the conventional structure function analysis fails to detect the power-law behavior. A Hilbert-based method was then performed in this work to identify the scaling behavior. A dual-power-law behavior separated by the viscosity wave number k_ν is observed with a limit scaling range, which is the result of this special system. This DPL belongs to the inverse cascade since it is on the left side of the injection scale, i.e., $k < k_R$, k_R is the body size wave number. As mentioned above for the traditional two-dimensional turbulence, there is no intermittent correction in the inverses cascade. On the contrary, due to several additional nonlinear interactions in this bacterial turbulence, the DPL is found experimentally to be intermittent. The intensity of the intermittency or multifractality is then characterized by a log-normal formula with measured $H_S = 0.91$ and $\mu_S = 0.26$ for the small-scale (high wave-number part $0.15 < k/k_R < 0.5$)

fluctuations, and $H_L = 0.73$ and $\mu_L = 0.17$ for the large-scale (low wave-number part $0.03 < k/k_R < 0.075$) fluctuations, showing that the former cascade is more intermittent than the latter one. This is also confirmed by the calculated singularity spectrum $f(\alpha)$. When comparing a continuum model of this active fluid system with the traditional two-dimensional Ekman-Navier-Stokes equation, there exist several additional nonlinear interactions that trigger the intermittency in the inverse cascade. A less intermittent large-scale fluctuation could be an effect of the fluid viscosity since it plays an important role when $k/k_R \leqslant 0.1$. We emphasize here that the observed DPL could not be universal since the bacterial turbulence depends on many different parameters, such as the species of the bacteria, the concentration, etc. It should be studied systematically by applying this Hilbert-based approach.

[1] U. Frisch, *Turbulence: The Legacy of A. N. Kolmogorov* (Cambridge University Press, Cambridge, UK, 1995).

[2] A. N. Kolmogorov, Dokl. Akad. Nauk SSSR **30**, 301 (1941).

[3] L. Richardson, *Weather Prediction by Numerical Process* (Cambridge University Press, Cambridge, England, 1922).

[4] F. Anselmet, Y. Gagne, E. J. Hopfinger, and R. A. Antonia, J. Fluid Mech. **140**, 63 (1984).

[5] K. R. Sreenivasan and R. A. Antonia, Annu. Rev. Fluid Mech. **29**, 435 (1997).

[6] Z. Warhaft, Annu. Rev. Fluid Mech. **32**, 203 (2000).

[7] D. Lohse and K.-Q. Xia, Annu. Rev. Fluid Mech. **42**, 335 (2010).

[8] R. Benzi, G. Paladin, A. Vulpiani, and G. Parisi, J. Phys. A **17**, 3521 (1984).

[9] G. Parisi and U. Frisch, Turbulence and predictability in geophysical fluid dynamics, *Proceedings of the International Summer School in Physics Enrico Fermi* (North-Holland, Amsterdam, 1985), p. 84.

[10] G. Batchelor and A. Townsend, Proc. R. Soc. London, Ser. A **199**, 238 (1949).

[11] C. Meneveau and K. R. Sreenivasan, J. Fluid Mech. **224**, 429 (1991).

[12] F. G. Schmitt and Y. Huang, *Stochastic Analysis of Scaling Time Series: From Turbulence Theory to Applications* (Cambridge University Press, Cambridge, England, 2016).

[13] A. N. Kolmogorov, J. Fluid Mech. **13**, 82 (1962).

[14] Z. S. She and E. Lévêque, Phys. Rev. Lett. **72**, 336 (1994).

[15] B. Dubrulle, Phys. Rev. Lett. **73**, 959 (1994).

[16] D. Schertzer and S. Lovejoy, J. Geophys. Res. **92**, 9693 (1987).

[17] S. Kida, J. Phys. Soc. Jpn. **60**, 5 (1991).

[18] R. Mantegna and H. E. Stanley, Nature **383**, 587 (1996).

[19] F. G. Schmitt, D. Schertzer, and S. Lovejoy, Appl. Stoch. Models Data Anal. **15**, 29 (1999).

[20] M. Li and Y. Huang, Physica A **406**, 222 (2014).

[21] R. Calif, F. G. Schmitt, and Y. Huang, Physica A **392**, 4106 (2013).

[22] Y. Huang, F. G. Schmitt, Z. Lu, and Y. Liu, J. Hydrol. **373**, 103 (2009).

[23] F. G. Schmitt, Y. Huang, Z. Lu, Y. Liu, and N. Fernandez, J. Mar. Sys. **77**, 473 (2009).

[24] H. Xia, D. Byrne, G. Falkovich, and M. Shats, Nat. Phys. **7**, 321 (2011).

[25] R. Kraichnan, Phys. Fluids **10**, 1417 (1967).

[26] G. Falkovich and K. R. Sreenivasan, Phys. Today **59**, 43 (2006).

[27] G. Boffetta and R. Ecke, Annu. Rev. Fluid Mech. **44**, 427 (2012).

[28] J. Paret, M. C. Jullien, and P. Tabeling, Phys. Rev. Lett. **83**, 3418 (1999).

[29] H. Kellay, X. L. Wu, and W. I. Goldburg, Phys. Rev. Lett. **80**, 277 (1998).

[30] H. Tan, Y. Huang, and J.-P. Meng, Phys. Fluids **26**, 015106 (2014).

[31] L. Wang and Y. Huang, J. Stat. Mech. (2015) P06018.

[32] Y. Huang, F. G. Schmitt, Z. Lu, P. Fougairolles, Y. Gagne, and Y. Liu, Phys. Rev. E **82**, 026319 (2010).

[33] K. Nam, E. Ott, T. M. Antonsen, Jr., and P. N. Guzdar, Phys. Rev. Lett. **84**, 5134 (2000).

[34] D. Bérnard, Europhys. Lett. **50**, 333 (2000).

[35] X.-L. Wu and A. Libchaber, Phys. Rev. Lett. **84**, 3017 (2000).

[36] C. M. Pooley, G. P. Alexander, and J. M. Yeomans, Phys. Rev. Lett. **99**, 228103 (2007).

[37] T. Ishikawa and T. J. Pedley, Phys. Rev. Lett. **100**, 088103 (2008).

[38] I. Rushkin, V. Kantsler, and R. E. Goldstein, Phys. Rev. Lett. **105**, 188101 (2010).

[39] T. Ishikawa, N. Yoshida, H. Ueno, M. Wiedeman, Y. Imai, and T. Yamaguchi, Phys. Rev. Lett. **107**, 028102 (2011).

[40] X. Chen, X. Dong, A. Be'er, H. L. Swinney, and H. P. Zhang, Phys. Rev. Lett. **108**, 148101 (2012).

[41] H. H. Wensink, J. Dunkel, S. Heidenreich, K. Drescher, R. E. Goldstein, H. Löwen, and J. M. Yeomans, Proc. Natl. Acad. Sci. USA **109**, 14308 (2012).

[42] J. Dunkel, S. Heidenreich, K. Drescher, H. H. Wensink, M. Bär, and R. E. Goldstein, Phys. Rev. Lett. **110**, 228102 (2013).

[43] D. Saintillan and M. J. Shelley, J. R. Soc. Interface **9**, 571 (2012).

[44] J. Dunkel, S. Heidenreich, M. Bär, and R. E. Goldstein, New J. Phys. **15**, 045016 (2013).

[45] R. Großmann, P. Romanczuk, M. Bar, and L. Schimansky-Geier, Phys. Rev. Lett. **113**, 258104 (2014).

[46] M. C. Marchetti, J. F. Joanny, S. Ramaswamy, T. B. Liverpool, J. Prost, M. Rao, and R. A. Simha, Rev. Mod. Phys. **85**, 1143 (2013).

[47] C. Dombrowski, L. Cisneros, S. Chatkaew, R. E. Goldstein, and J. O. Kessler, Phys. Rev. Lett. **93**, 098103 (2004).

[48] K.-A. Liu and L. I, Phys. Rev. E **86**, 011924 (2012).

[49] The Kolmogorov scale or viscosity scale is estimated as $\ell_\nu = (\nu^3/\epsilon)^{3/4}$, in which ν is the viscosity of the fluid and ϵ is the energy dissipation rate. A typical value of ℓ_ν in the ocean is $0.3 \sim 2$ mm. A typical ℓ_ν in a pipe flow is around $25\,\mu$m with a diameter 50 mm and a velocity 1.8 m/s. For the current database, it is reasonable to take the viscosity scale as $\ell_\nu \simeq 50\,\mu$m.

[50] R. Benzi, S. Ciliberto, R. Tripiccione, C. Baudet, F. Massaioli, and S. Succi, Phys. Rev. E **48**, R29(R) (1993).

[51] R. Benzi, S. Ciliberto, C. Baudet, and G. Chavarria, Physica D **80**, 385 (1995).

[52] R. Benzi, S. Ciliberto, C. Baudet, G. Chavarria, and R. Tripiccione, Europhys. Lett. **24**, 275 (1993).

[53] A. Arneodo, C. Baudet, F. Belin, R. Benzi, B. Castaing, B. Chabaud, R. Chavarria, S. Ciliberto, R. Camussi, and F. Chilla, Europhys. Lett. **34**, 411 (1996).

[54] Y. Huang, F. G. Schmitt, J.-P. Hermand, Y. Gagne, Z. Lu, and Y. Liu, Phys. Rev. E **84**, 016208 (2011).

[55] Y. Huang, L. Biferale, E. Calzavarini, C. Sun, and F. Toschi, Phys. Rev. E **87**, 041003(R) (2013).

[56] N. E. Huang, Z. Shen, S. Long, M. Wu, H. Shih, Q. Zheng, N. Yen, C. Tung, and H. Liu, Proc. R. Soc. London, Ser. A **454**, 903 (1998).

[57] Y. Huang, F. G. Schmitt, Z. Lu, and Y. Liu, Europhys. Lett. **84**, 40010 (2008).

[58] N. E. Huang, Z. Shen, and S. Long, Annu. Rev. Fluid Mech. **31**, 417 (1999).

[59] L. Cohen, *Time-Frequency Analysis* (Prentice Hall PTR, Englewood Cliffs, NJ, 1995).

[60] G. Rilling, P. Flandrin, and P. Gonçalvès, IEEE-EURASIP Workshop on Nonlinear Signal and Image Processing (2003).

[61] Y. Huang, F. G. Schmitt, and Y. Gagne, J. Stat. Mech. (2014) P05002.

[62] P. Flandrin and P. Gonçalvès, Int. J. Wavelets, Multires. Info. Proc. **02**, 477 (2004).

[63] Q. Chen, N. E. Huang, S. Riemenschneider, and Y. Xu, Adv. Comput. Math. **24**, 171 (2006).

[64] N. E. Huang, M. L. Wu, S. R. Long, S. S. P. Shen, W. Qu, P. Gloersen, and K. L. Fan, Proc. R. Soc. London, Ser. A **459**, 2317 (2003).

[65] Z. Wu and N. E. Huang, Proc. R. Soc. London, Ser. A **460**, 1597 (2004).

[66] G. Rilling and P. Flandrin, IEEE Trans. Signal Proc. **56**, 85 (2008).

[67] Y.-H. Wang, C.-H. Yeh, H.-W. V. Young, K. Hu, and M.-T. Lo, Physica A **400**, 159 (2014).

[68] N. E. Huang, Z. Wu, S. Long, K. Arnold, X. Chen, and K. Blank, Adv. Adapt. Data Anal. **01**, 177 (2009).

[69] Q. Zhou, Y. Huang, Z. Lu, Y. Liu, and R. Ni, J. Fluid Mech. **786**, 294 (2015).

[70] A. Sokolov and I. S. Aranson, Phys. Rev. Lett. **103**, 148101 (2009).

[71] S. Rafaï, L. Jibuti, and P. Peyla, Phys. Rev. Lett. **104**, 098102 (2010).

[72] H. M. López, J. Gachelin, C. Douarche, H. Auradou, and E. Clément, Phys. Rev. Lett. **115**, 028301 (2015).

[73] See http://damtp.cam.ac.uk/user/gold/datarequests.htm

[74] See http://perso.ens-lyon.fr/patrick.flandrin/emd.html

[75] See https://github.com/lanlankai